Nanoscale

PAPER

View Article Online
View Journal | View Issue

Cite this: *Nanoscale*, 2025, **17**, 6562

Controllable magnetism and an anomalous Hall effect in $(Bi_{1-x}Sb_x)_2Te_3$-intercalated $MnBi_2Te_4$ multilayers

Peng Chen,†[a,b,c] Jieyi Liu, *†[d,e] Yifan Zhang,†[a] Puyang Huang,[a] Jack Bollard,[d,e] Yiheng Yang,[e] Ethan L. Arnold,[d,e] Xinqi Liu,[f,g] Qi Yao,[f,g] Fadi Choueikani,[h] Gerrit van der Laan,[d] Thorsten Hesjedal[d,e] and Xufeng Kou *[a,f]

Received 30th December 2024,
Accepted 8th February 2025

DOI: 10.1039/d4nr05486e

rsc.li/nanoscale

$MnBi_2Te_4$-based superlattices not only enrich the materials family of magnetic topological insulators, but also offer a platform for tailoring magnetic properties and interlayer magnetic coupling through the strategic insertion layer design. Here, we present the electrical and magnetic characterization of $(Bi_{1-x}Sb_x)_2Te_3$-intercalated $MnBi_2Te_4$ multilayers grown by molecular beam epitaxy. By precisely adjusting the Sb-to-Bi ratio in the spacer layer, the magneto-transport response is modulated, unveiling the critical role of Fermi level tuning in optimizing the anomalous Hall signal and reconfiguring the magnetic ground state. Moreover, by varying the interlayer thickness, tunable magnetic coupling is achieved, enabling precise control over ferromagnetic and antiferromagnetic components. These findings pave the way for the exploration of versatile magnetic topological phases in quantum materials systems.

Introduction

Magnetic topological insulators (MTIs), characterized by the coexistence of a topologically nontrivial band structure and time-reversal symmetry breaking induced by magnetic order, have catalyzed significant advancements in the realms of topological quantum physics[1–5] and device applications.[6–11] Conventionally, the incorporation of magnetic dopants into the topological insulator framework has been validated as an effective approach to establishing robust magnetic order. However, the inhomogeneous distribution of dopants and the localized coupling of the magnetic elements restrict the realization of quantum phenomena to ultra-low temperatures, far below their magnetic transition temperature.[4,5,12] Alternatively, in the pursuit of uniform magnetization in the intrinsic MTIs, $Mn(Bi, Sb)_2(Te, Se)_4$ has emerged as a promising avenue. These materials feature a planar arrangement of covalently bonded Mn atoms within the X–Y–X–Mn–X–Y–X (X = Se or Te, and Y = Bi or Sb) septuple layers (SLs).[12–14] In this context, the combination of strong spin–orbit coupling and spontaneous interlayer magnetic coupling has provided the observations of the quantum anomalous Hall effect and quantum-metric-induced nonlinear transport in exfoliated $MnBi_2Te_4$ flakes at elevated temperatures, manifesting the advantages of intrinsic MTIs to implement topological quantum computing and energy-efficient spintronic devices with quantized transport features.[15–20]

More importantly, considering that the $Mn(Bi, Sb)_2(Te, Se)_4$ system hosts both intralayer ferromagnetic (FM) and interlayer antiferromagnetic (AFM) coupling, it was hence proposed that the insertion of a spacer layer between neighboring SLs would modulate the strength of each contribution.[21] For instance, it was found that non-magnetic intercalation enables tuning of the Anderson AFM coupling between MBTs by controlling the layer thickness.[22–26] Likewise, a magnetic spacer (*e.g.*, MnTe) is able to stabilize the interlayer AFM coupling of the $MnBi_2Te_4$ layers through the exchange-spring effect and the magneto-resistance response can be controlled *via* the MnTe layer thickness.[27] These new breakthroughs underscore the potential of heterostructure engineering for broadening the research scope of $MnBi_2Te_4$-based materials systems.[22–27]

[a]*School of Information Science and Technology, ShanghaiTech University, Shanghai, 201210, China. E-mail: kouxf@shanghaitech.edu.cn*
[b]*Shanghai Institute of Microsystem and Information Technology, Chinese Academy of Sciences, Shanghai 200050, China*
[c]*University of Chinese Academy of Sciences, Beijing 101408, China*
[d]*Diamond Light Source, Harwell Science and Innovation Campus, Didcot OX11 0DE, UK. E-mail: jieyi.liu@diamond.ac.uk*
[e]*Department of Physics, Clarendon Laboratory, University of Oxford, Oxford OX1 3PU, UK*
[f]*ShanghaiTech Laboratory for Topological Physics, ShanghaiTech University, Shanghai 201210, China*
[g]*School of Physical Science and Technology, ShanghaiTech University, Shanghai, 201210, China*
[h]*Synchrotron SOLEIL, L'Orme des Merisiers, Départementale 128, 91190 Saint-Aubin, France*
†These authors contributed equally to this work.

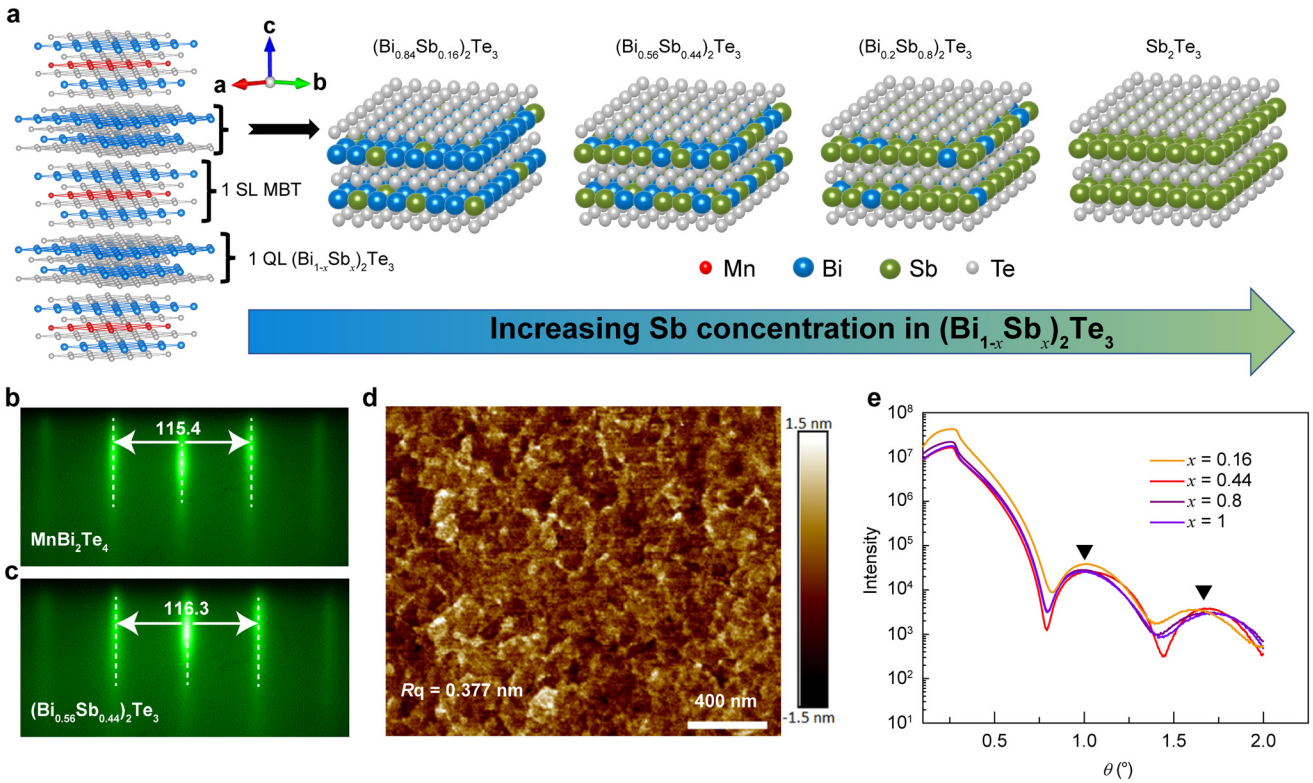

Fig. 1 Characterization of the MBE-grown $[MnBi_2Te_4]_3[(Bi_{1-x}Sb_x)_2Te_3]_2$ multilayers. (a) Schematic showing the multilayer structures with varying Sb contents in the $(Bi_{1-x}Sb_x)_2Te_3$ spacer layer. (b) and (c) *In situ* RHEED patterns after the growth of the $MnBi_2Te_4$ (top panel) and $(Bi_{0.56}Sb_{0.44})_2Te_3$ (bottom panel) layers. The sharp 2D strips persist throughout the sample growth. (d) Atomic force microscopy image of the as-grown $[MnBi_2Te_4]_3[Sb_2Te_3]_2$ sample with an average R_q value of 0.377 nm across a 2 μm × 1.6 μm area. (e) X-ray reflectivity plots of four $(Bi_{1-x}Sb_x)_2Te_3$-intercalated films (x = 0.16, 0.44, 0.8, and 1), displaying pronounced oscillatory Kiessig fringes.

Inspired by the above strategy, in this article, we present the synthesis of $(Bi_{1-x}Sb_x)_2Te_3$-intercalated $MnBi_2Te_4$ thin films *via* molecular beam epitaxy (MBE). By varying the Sb concentration, we demonstrate a precise tuning of the Fermi level position across the Dirac point, which triggers non-monotonic variations in both the zero-field anomalous Hall resistance and the saturation field, with the x = 0.44 sample achieving the most favorable characteristics. Correspondingly, X-ray magnetic circular dichroism (XMCD) measurements reveal an enhanced magnetic moment at this specific composition, suggesting a positive correlation between the FM order and the anomalous Hall responses. Furthermore, by fine-tuning the thickness of the $(Bi_{1-x}Sb_x)_2Te_3$ spacer layer, we observe the transition of the system's ground state between the AFM and FM phases. Our work not only advances the frontier of intrinsic magnetic topological insulators but also provides new insights into the exploration of novel physical phenomena in $MnBi_2Te_4$-based systems.

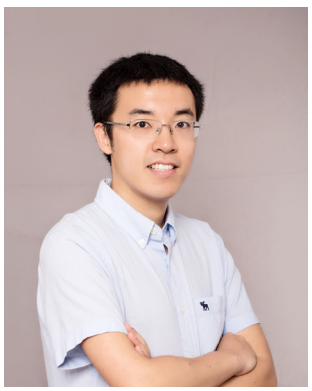

Xufeng Kou

Xufeng Kou is currently a full professor in the School of Information Science and Technology (SIST) at ShanghaiTech University, China. He received his PhD at the University of California Los Angeles (UCLA) in 2015 under the supervision of Professor Kang L. Wang. After completing his postdoctoral research at UCLA, he joined ShanghaiTech in 2016 and has led several research programs including topological quantum materials, spintronics, and cryogenic electronics. Prof. Kou is a senior member of IEEE, and he is a recipient of the Qualcomm Innovation Fellowship and several national research awards in China.

Main text

Fig. 1a illustrates the proposed $MnBi_2Te_4/(Bi_{1-x}Sb_x)_2Te_3/MnBi_2Te_4/(Bi_{1-x}Sb_x)_2Te_3/MnBi_2Te_4$ multilayer structure where the two non-magnetic $(Bi_{1-x}Sb_x)_2Te_3$ spacer layers are embedded within the 3-SL $MnBi_2Te_4$ matrix. Experimentally, two-inch $Al_2O_3(0001)$ wafers were chosen as the substrate as the absence of dangling bonds at the substrate surface would warrant a uniform surface energy distribution and facilitate

the van der Waals epitaxial growth mode. Based on our previous growth protocols,[27,28] the $MnBi_2Te_4$ septuple layer was obtained by post-annealing one quintuple layer (QL) of Bi_2Te_3 and one monolayer of MnTe, and the Sb-to-Bi ratio in the $(Bi_{1-x}Sb_x)_2Te_3$ spacer layer was calibrated *via* a beam flux monitor (BFM). During sample growth, reflection high-energy electron diffraction (RHEED) was used to *in situ* monitor the growth process. As exemplified in Fig. 1b and c, the sharp streaky RHEED patterns persist during the growth of both the $MnBi_2Te_4$ and $(Bi_{0.56}Sb_{0.44})_2Te_3$ layers, revealing a two-dimensional epitaxial growth mode. The *d*-spacing length between the 1st-order streaks (*i.e.*, which is related to the reciprocal lattice unit, as marked by the white arrowhead line) is found to expand from 115.4 ($MnBi_2Te_4$) to 116.3 ($(Bi_{0.56}Sb_{0.44})_2Te_3$), reflecting with the in-plane lattice constant difference between $(Bi_{0.56}Sb_{0.44})_2Te_3$ (4.33 Å) and $MnBi_2Te_4$ (4.37 Å).[29,30] Meanwhile, the atomic force microscopy (AFM) image shown in Fig. 1d visualizes an atomically smooth surface of the as-grown multilayer film after a dedicated post-annealing process, with the quadratic mean surface roughness R_q = 0.377 nm (*i.e.*, less than one SL/QL thickness) captured from a 2 μm × 1.6 μm area. Besides, Fig. 1e displays the measured X-ray reflectivity (XRR) curves of four $[MnBi_2Te_4]_3[(Bi_{1-x}Sb_x)_2Te_3]_2$ samples (x = 0.16, 0.44, 0.8, and 1), all of which exhibit pronounced Kiessig fringes with identical equally-spaced oscillatory characteristics. By further applying the Bragg equation ($2d \sin \Delta\theta = n\lambda$, where d is the interplanar spacing, λ = 1.5406 Å is the incident X-ray wavelength, θ is the angle between the incident X-ray and the corresponding crystal plane, and n is the diffraction order, respectively[31]), the film thicknesses of these four samples were found to be 6.6 nm, which falls within the error margin of the theoretical value of 6.1 nm. Therefore, the above material characterization studies confirm the high quality of the MBE-grown single-crystal $[MnBi_2Te_4]_3[(Bi_{1-x}Sb_x)_2Te_3]_2$ thin films, offering a reliable foundation for the present study.

It is known that the band structure and corresponding electrical properties of the ternary topological insulator $(Bi_{1-x}Sb_x)_2Te_3$ can be well-controlled *via* the Sb-to-Bi ratio.[29] Under such conditions, it is expected that the change of x may also enable the tailoring of the $(Bi_{1-x}Sb_x)_2Te_3$-intercalated $MnBi_2Te_4$ system. For this purpose, a series of μm-sized six-terminal Hall-bar devices were fabricated out of the $[MnBi_2Te_4]_3[(Bi_{1-x}Sb_x)_2Te_3]_2$ multilayer films using a standard nano-fabrication process. Afterward, temperature-dependent magneto-transport measurements were carried out (Fig. 2a), where a fixed AC current (*i.e.*, whose amplitude was kept at I_0 = 1 μA, and the lock-in frequency was set to 18.7 Hz) was applied along the x-direction and the perpendicular magnetic field $\mu_0 H$ was varied between −10 T and +10 T. Fig. 2b1–4 present

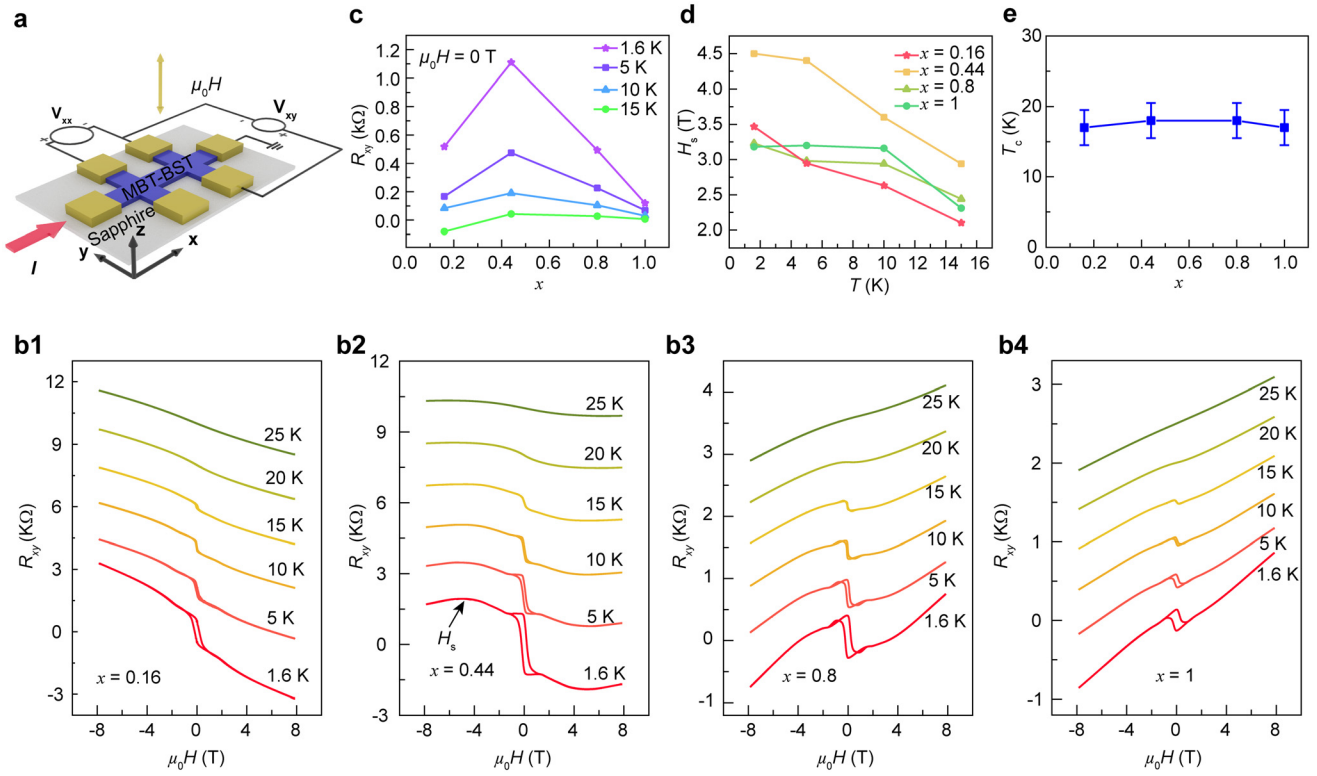

Fig. 2 Temperature-dependent anomalous Hall responses of MBE-grown $[MnBi_2Te_4]_3[(Bi_{1-x}Sb_x)_2Te_3]_2$ thin films. (a) Schematic of a six-terminal Hall-bar device and magneto-transport measurement setup. The current I was applied along the x-direction and the external magnetic field $\mu_0 H$ was applied along the z-direction. (b1)–(b4) Temperature-dependent anomalous Hall resistances of x = 0.16, 0.44, 0.8, and 1 samples from T = 1.6 and 25 K. (c) Saturation magnetic field H_s extracted from the measured anomalous Hall resistance curves. (d) Zero-field Hall resistance obtained at different temperatures. (e) Critical transition temperatures (T_c) of $(Bi_{1-x}Sb_x)_2Te_3$-intercalated $MnBi_2Te_4$ samples (x = 0.16, 0.44, 0.8 and 1).

the measured Hall resistance (R_{xy}) results of the four samples with x = 0.16, 0.44, 0.8, and 1. With the increase of the Sb content x in the $(Bi_{1-x}Sb_x)_2Te_3$ spacer layer, the slope of R_{xy} in the high-field region (*i.e.*, where the ordinary Hall effect dominates at $|\mu_0 H| > 6$ T) experiences a negative-to-positive transition, which suggests that the major carrier type changes from the electron (n-type) to hole (p-type), and the Fermi level is tuned across the Dirac point between x = 0.16 and 0.44. In alignment with such an Sb-induced ambipolar effect, it is seen from Fig. 2c that the zero-field anomalous Hall resistance (*i.e.*, indicative of the spontaneous FM order) exhibits a non-monotonic correlation with the Sb-to-Bi ratio, with the largest value of R_{xy} = 1.1 kΩ observed in the x = 0.44 sample (*e.g.*, which is 10 times larger than the x = 1 counterpart at T = 1.6 K). This non-monotonic trend may be associated with the van Vleck mechanism, which is the second-order perturbative coupling between the localized spins introduced by Mn atoms and the electrons of the topological surface states within the bulk bandgap.[32] When the surface state contribution is maximized in the x = 0.44 case, robust out-of-plane magnetization could be developed from the large van Vleck spin susceptibility, thereby leading to an enlarged R_{xy} resistance under zero-field conditions.[32–34] Concurrently, the saturation field is also found to reach its maximal value at H_s = 4.5 T in the $[MnBi_2Te_4]_3[(Bi_{0.56}Sb_{0.44})_2Te_3]_2$ sample, implying the optimization of the interlayer AFM-type Anderson exchange coupling strength (Fig. 2d), which may arise from the modification of Mn-related spin texture through the interaction between localized magnetic moments and electrons,[35,36] as will be analyzed in the following sections. In addition, the gradual disappearance of hysteresis anomalous Hall loops in $[MnBi_2Te_4]_3[(Bi_{1-x}Sb_x)_2Te_3]_2$ samples at T = 15 K–20 K (Fig. 2e) indicates that the critical transition temperature is slightly higher than that of their Bi_2Te_3-intercalated counterparts.[23,24]

To further understand the effect of the intercalated $(Bi_{1-x}Sb_x)_2Te_3$ layer on the magnetic properties of the $MnBi_2Te_4$-based multilayer system, we carried out low-temperature X-ray magnetic circular dichroism (XMCD) measurements on the x = 0.44 and 1 samples (*i.e.*, both films were capped with amorphous Te layers to prevent surface oxidation), where both the incident beam and magnetic field were applied along the out-of-plane direction of the films, and the magnetic moment of Mn was probed along the z-axis. Fig. 3a and b show the X-ray absorption spectra (XAS) of the Mn-$L_{2,3}$ edges, which were averaged over positive and negative circular polarizations at $\mu_0 H_z$ = +6 T. It is obvious that both samples display

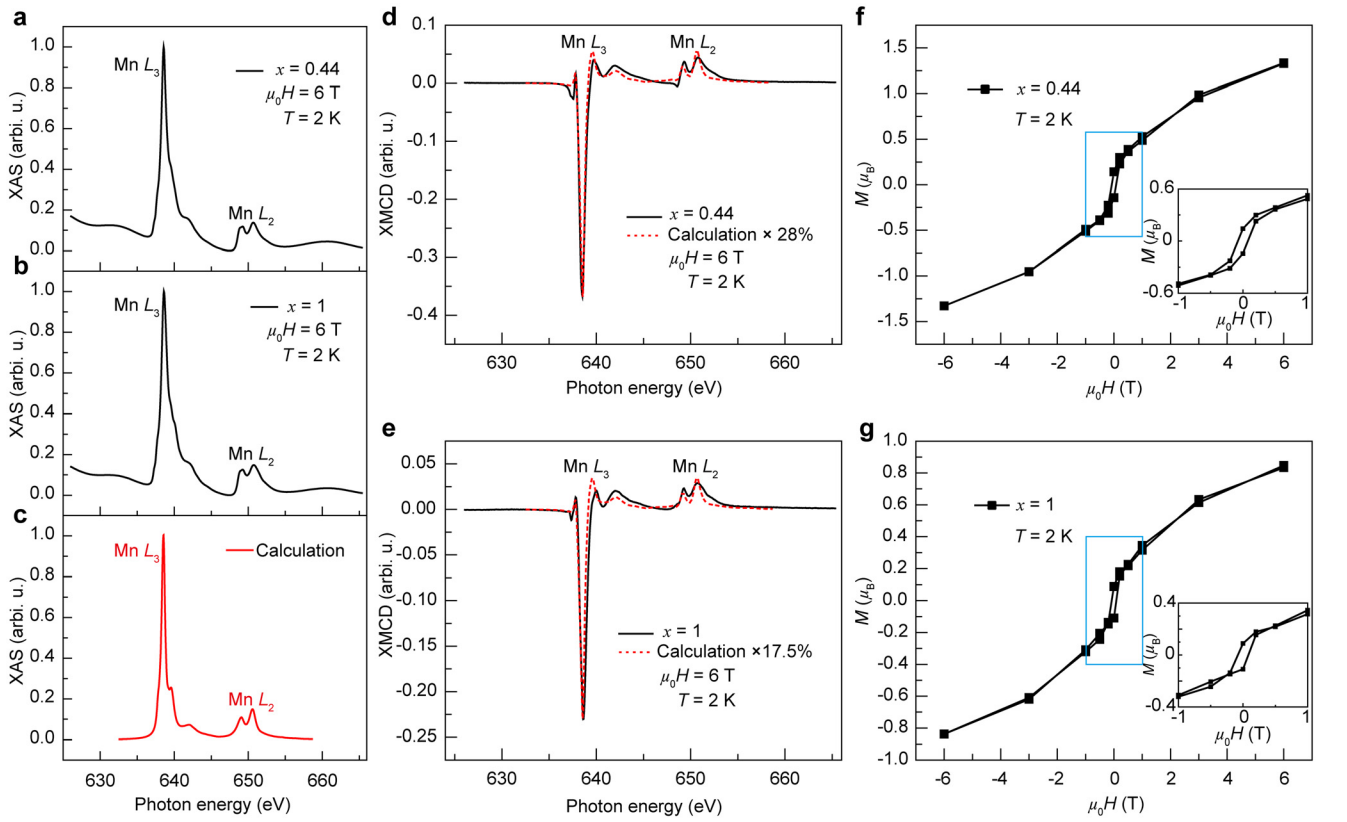

Fig. 3 XAS and XMCD results at the Mn $L_{2,3}$ edges of the x = 0.44 and 1 samples. All measurements were performed at T = 2 K, with both the X-ray beam and the applied magnetic field perpendicular to the sample plane. (a) and (b), XAS spectra at 6 T for x = 0.44 (a) and x = 1 (b) samples. (c), Calculated absorption spectrum based on a hybridized ground state of Mn. (d) and (e) XMCD spectra at 6 T for x = 0.44 (d) and 1 (e) samples. The calculated dichroic spectrum (red dashed lines) was rescaled and overlaid on the experimental data. (f)and (g), Hysteresis XMCD loops with non-zero spin moments observed in both x = 0.44 (f) and x = 1 (g) samples. Inset: a close-up view of the hysteresis features within ±1 T.

an oxygen-free spectrum in close resemblance to those obtained from *in situ* cleaved $MnBi_2Te_4$ single crystals,[20,37] hence allowing for high-quality detection in the total-electron yield mode. In contrast to the calculated spectrum of a localized d^5 ground state,[38] the recorded experimental line shapes are in good agreement with an Anderson impurity calculation of a mixed state of Mn,[39] which contains d^4, d^5, and d^6 characteristics, as shown in Fig. 3c. In this regard, our observations may confirm that the Mn atoms in $MnBi_2Te_4$ with a $(Bi_{1-x}Sb_x)_2Te_3$ spacer system have a hybridized ground state. Subsequently, by subtracting the high-field XAS data with opposite circular polarizations, the corresponding XMCD spectra were recorded. As visualized in Fig. 3d and e, the dichroism at both Mn L_3 and L_2 edges shows a clear net magnetization at +6 T. By rescaling the calculated XMCD spectrum of the hybridized ground state that has a saturated spin moment of $4.75\mu_B$ per Mn atom in theory,[20,40,41] we obtained a good match with the experimental data when the magnitude of the calculated spectrum (red dashed lines) is scaled down to 28% (x = 0.44) and 17.5% (x = 1). The deviation of magnetic moments of the epitaxial thin films from the ideal bulk form may be attributed to the weakened intra-/inter-layer exchange interaction as well as the existence of structural defects in the MBE-grown samples.[27,42] On this basis, the high-field spin magnetic moments of the x = 0.44 and 1 samples at $\mu_0 H_z$ = +6 T are estimated to be 1.33 and $0.83\mu_B$ per Mn, respectively, similar to other reports.[40] Following this principle, a series of XMCD spectra were recorded under different magnetic fields, effectively yielding a magnetic hysteresis loop within the instrument limit of ±6 T. As illustrated in Fig. 3f and g. a soft loop opening is revealed in both films, accompanied by a non-zero remnant spin magnetization at zero field, with values of $0.14\mu_B$ per Mn (x = 0.44) and $0.09\mu_B$ per Mn (x = 1). The smaller magnetic moment probed in the x = 1 sample may be caused by the increased magnetic fluctuations in the Sb_2Te_3 insertion layer.[43] Here, we need to point out that the orbital moment of Mn is neglected in this discussion due to its negligible magnitude compared to the spin moment, which is common in 3d magnetic elements with nearly half-filled shells.[44] Consequently, these results confirm that both samples exhibit a non-zero net FM order, with a stronger magnetic moment observed in the x = 0.44 case, which is consistent with the magneto-transport results.

Apart from the Sb-to-Bi ratio, the insertion layer thickness may serve as another tuning parameter in regulating the magnetic coupling between the $MnBi_2Te_4$ layers. Accordingly, based on the optimized $MnBi_2Te_4/(Bi_{0.56}Sb_{0.44})_2Te_3/MnBi_2Te_4/(Bi_{0.56}Sb_{0.44})_2Te_3/MnBi_2Te_4$ structure (Sample A), we have grown two additional samples, namely $MnBi_2Te_4$/2QL-$(Bi_{0.56}Sb_{0.44})_2Te_3/MnBi_2Te_4$ (Sample B) and $MnBi_2Te_4$/3QL-$(Bi_{0.56}Sb_{0.44})_2Te_3/MnBi_2Te_4$ (Sample C). Fig. 4a–c summarize the temperature-dependent anomalous Hall resistance R_{xy}^{AHE} of

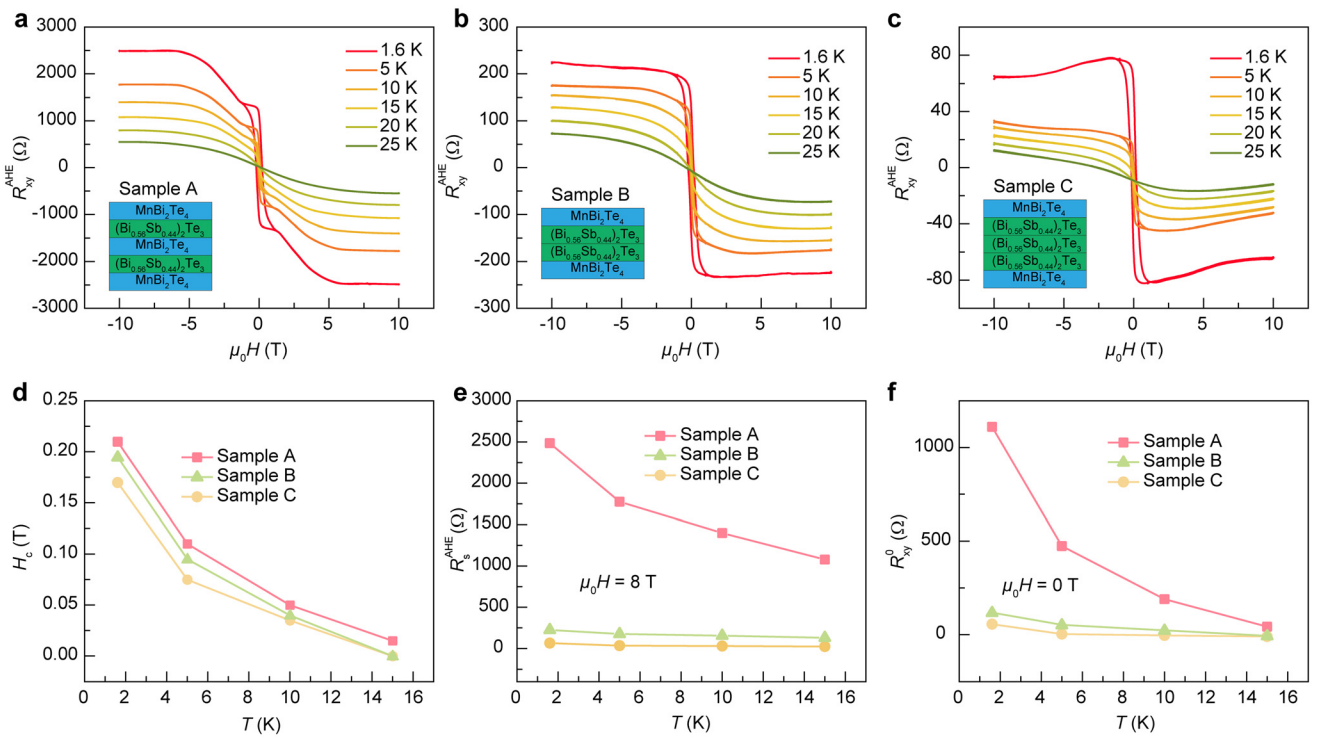

Fig. 4 Temperature-dependent anomalous Hall resistance in $(Bi_{0.56}Sb_{0.44})_2Te_3$-intercalated $MnBi_2Te_4$ multilayers with different spacer layer thicknesses and stacking order. (a)–(c) Temperature-dependent anomalous Hall resistance of $MnBi_2Te_4/(Bi_{0.56}Sb_{0.44})_2Te_3/MnBi_2Te_4/(Bi_{0.56}Sb_{0.44})_2Te_3/MnBi_2Te_4$ (Sample A), $MnBi_2Te_4$/2QL-$(Bi_{0.56}Sb_{0.44})_2Te_3/MnBi_2Te_4$ (Sample B), and $MnBi_2Te_4$/3QL-$(Bi_{0.56}Sb_{0.44})_2Te_3/MnBi_2Te_4$ (Sample C). (d)–(f), Corresponding coercive field H_c (d), saturated anomalous Hall resistance R_s^{AHE} (e), and zero-field anomalous Hall resistance R_{xy}^0 (f) obtained from the measured data in (a)–(c).

these three samples, in which the linear backgrounds contributed from the ordinary Hall effect were subtracted from the measured Hall data. At the base temperature of T = 1.6 K (*i.e.*, which is well below the Néel temperature of $MnBi_2Te_4$), the R_{xy}^{AHE} contour of Sample A resembles the reported odd-layered $MnBi_2Te_4$ reference sample, where the increase of the R_{xy}^{AHE} slope in the $\mu_0 H \subseteq [2\ T, 4.5\ T]$ region and the high-field saturation behavior reflect the spin-flop transition of an A-type AFM system.[45,46] In contrast, both Samples B and C display typical square-shaped hysteresis R_{xy}^{AHE} loops, epitomizing the dominant FM order at low temperatures. In order to quantitatively compare these three samples, we plotted the temperature-dependent coercive field, H_c (Fig. 4d), high-field saturated anomalous Hall resistance, R_s^{AHE} (Fig. 4e), and zero-field Hall resistance, R_{xy}^0 (Fig. 4f). Intriguingly, while the coercive fields of all the three samples are similar in magnitude and follow the same temperature evolution trend, the R_s^{AHE} (R_{xy}^0) values reduce by 91% (89%) or 97% (95%) as long as the center $MnBi_2Te_4$ layer in Sample A is removed (*e.g.*, Sample B) or replaced by the non-magnetic layer (*e.g.*, Sample C). Considering that the interlayer AFM-type Anderson superexchange coupling strength has a negative correlation with the spacing between adjacent $MnBi_2Te_4$ layers,[22,23] the intercalated 2QL and 3QL-$(Bi_{0.56}Sb_{0.44})_2$ thickness may exceed the critical length of AFM coupling. As a result, the top and bottom $MnBi_2Te_4$ layers in Samples B and C no longer interact with each other, leaving the spin configuration of the system mainly shaped by the intra-layer coupling of the covalently-bonded Mn layer within the $MnBi_2Te_4$ SL matrix. Therefore, these results validate the manipulation of the FM *versus* AFM coupling through the insertion layer thickness modulation.

Conclusion

In conclusion, our systematic investigations of $(Bi_{1-x}Sb_x)_2Te_3$-intercalated $MnBi_2Te_4$ thin films have unveiled the pivotal role of the Sb-to-Bi ratio in the spacer layer in modulating the FM and AFM couplings, which in turn have led to the optimization of the anomalous Hall effect. Through comprehensive magneto-transport and XMCD measurements, we have provided compelling evidence of the interplay between elemental composition, spacer layer thickness, and the enhancement of magnetic properties. Our findings offer a blueprint for the design of magnetic topological materials with tailored functionalities and may open new avenues for future innovations in the realm of quantum material-based spintronic applications.

Methods

Sample growth and characterization

$(Bi_{1-x}Sb_x)_2Te_3$-intercalated $MnBi_2Te_4$ multilayers were deposited on $Al_2O_3(0001)$ substrates using molecular beam epitaxy at a base pressure of 10^{-10} torr. The substrate was first annealed at 570 °C, and high-quality Mn (99.9998%), Bi (99.99999%), Sb (99.99999%), and Te (99.99999%) materials were subsequently co-evaporated from standard Knudsen and cracker cells. To obtain a stoichiometric septuple-layer $MnBi_2Te_4$ structure, monolayers of Bi_2Te_3 and MnTe were grown at 200 °C and 370 °C, respectively, followed by a post-annealing process at 390 °C. The $(Bi_{1-x}Sb_x)_2Te_3$ insertion layer was also grown at 200 °C. Reflection high-energy electron diffraction and a beam flux monitor were used to monitor the growth process. After sample growth, the thickness of the thin films was calibrated using X-ray reflectivity.

Device fabrication

The six-terminal Hall bar devices were fabricated using a standard nano-fabrication process in a clean room under ISO-5 and ISO-6 level conditions. The $(Bi_{1-x}Sb_x)_2Te_3$-inserted $MnBi_2Te_4$ multilayer samples were firstly coated with an AZ5214 photoresist (thickness of 1.4 μm) before being exposed using laser photolithography MLA150. Subsequently, six-terminal Hall bar structures were obtained by Ar-ion etching. Finally, Ti/Au electrodes (thickness of 160 nm) were deposited using an e-beam evaporation process.

Transport measurement

The magneto-transport measurements of $[MnBi_2Te_4]_3[(Bi_{1-x}Sb_x)_2Te_3]_2$ multilayers were carried out in He^4 refrigerators (Oxford Teslatron PT system), which offer a base temperature of 1.5 K and a magnetic field of up to ±14 T. The current amplitude was fixed at 1 μA and the transport signal was captured using the standard lock-in measurement technique, with a tunable lock-in frequency between 1 and 1000 Hz.

X-ray magnetic circular dichroism

X-ray absorption spectroscopy (XAS) and X-ray magnetic circular dichroism (XMCD) measurements were performed using the CroMag endstation of the DEIMOS beamline at the SOLEIL synchrotron in Paris, France, at a base temperature of 2 K with an applied magnetic field up to ±6 T along the beam direction. The incident X-ray beam was along the out-of-plane direction of the films. XAS was carried out in the total-electron yield mode at the Mn $L_{2,3}$ edges. XMCD spectra were recorded by subtracting the absorption spectra recorded with opposite helicities of the incident X-ray beam, which was aligned either parallel or antiparallel to the applied magnetic field. The measured XMCD was compared with the results of atomic multiplet calculations. In localized many-electron systems, transitions are of the type $d^N \rightarrow p^5d^{N+1}$ for $L_{2,3}$ edges of d-metals. The wave functions of the initial- and final-state configurations are calculated in intermediate coupling using an atomic Hartree–Fock (HF) code with relativistic correction, where the spin–orbit and electrostatic interactions appear on an equal footing.[47–49] Crystal- and ligand-field interactions are included in the multiplet code by using symmetry considerations. Furthermore, charge-transfer interactions are included using the intra-atomic Coulomb interaction, the so-called Hubbard U for a $3d^N$ ground state, where $U = E(3d^{N-1}) +$

$E(3d^{N+1}) - 2E(3d^N)$, together with the core-valence Coulomb interaction Q, and the ligand-to-metal charge transfer $\Delta = E(3d^{N+1}\underline{L}) - E(3d^N)$, where $\underline{L}$ denotes a hole on the ligand. Fig. 3 shows the calculated Mn $L_{2,3}$ XAS and XMCD spectra for a hybridized ground state with 16% d^4, 58% d^5, and 26% d^6 character, which has a spin moment of 4.75μ_B per Mn. Details about the theoretical framework, assumptions, and computational methods of multiplet calculations and similar computational methods for 2p X-ray absorption spectroscopy of 3d transition metal systems have also been recently described and discussed in a previous report.[50]

Author contributions

X. F. Kou conceived the experiment. X. F. Kou and J. Y. Liu supervised the study. P. Chen, Y. F. Zhang, and X. Q. Liu grew the samples, performed material characterization, and conducted the transport measurements. P. Chen, Y. F. Zhang, P. Y. Huang, J. Y. Liu, and Q. Yao analyzed magneto-transport data. J. Y. Liu, J. Bollard, Y. H. Yang, E. Arnold, F, Choueikani, G. van der Laan, and T. Hesjedal contributed to the X-ray absorption spectroscopy (XAS) and X-ray magnetic circular dichroism (XMCD) measurements. G. van der Laan and J. Y. Liu simulated the corresponding theoretical XMCD results. P. Chen, J. Y. Liu, and X. F. Kou wrote the manuscript. All authors discussed the results and commented on the manuscript.

Data availability

All data needed to evaluate the conclusions in the paper are present in the paper and/or the ESI.† Any additional datasets, analysis details, and materials recipes are available upon request.

Conflicts of interest

The authors declare no competing financial interests.

Acknowledgements

This work was sponsored by the National Key R&D Program of China (grant no. 2023YFB4404000), the National Natural Science Foundation of China (grant no. 92164104), the Major Project of Shanghai Municipal Science and Technology (grant no. 2018SHZDZX02), the Shanghai Engineering Research Center of Energy Efficient and Custom AI IC, and the ShanghaiTech Material Device and Soft Matter Nano-fabrication Labs (SMN180827). The authors acknowledge SOLEIL for the provision of synchrotron radiation facilities (proposal number: 20231721). X. K. acknowledges support from the Open Fund of the State Key Laboratory of Infrared Physics and the Shanghai Oriental Leading Talent Program. E. L. A. acknowledges a Diamond-EPSRC studentship (2887640 and EP/W524311/1). J. B. acknowledges a Diamond-EPSRC studentship (2606404, EP/R513295/1 and EP/T517811/1).

References

1 Y. Tokura, K. Yasuda and A. Tsukazaki, Magnetic topological insulators, *Nat. Rev. Phys.*, 2019, **1**, 126–143.
2 Q. Yao, Y. Ji, P. Chen, Q.-L. He and X. Kou, Topological insulators-based magnetic heterostructures, *Adv. Phys.: X*, 2021, **6**, 1870560.
3 J. Liu and T. Hesjedal, Magnetic topological insulator heterostructures: A review, *Adv. Mater.*, 2023, **35**, 2102427.
4 X. Kou, *et al.*, Scale-invariant quantum anomalous Hall effect in magnetic topological insulators beyond the two-dimensional limit, *Phys. Rev. Lett.*, 2014, **113**, 137201.
5 C. Z. Chang, *et al.*, Experimental Observation of the Quantum Anomalous Hall Effect in a Magnetic Topological Insulator, *Science*, 2013, **340**, 167–170.
6 B. Cui, *et al.*, Low–Power and Field–Free Perpendicular Magnetic Memory Driven by Topological Insulators, *Adv. Mater.*, 2023, **35**, 2302350.
7 H. Wu, *et al.*, Magnetic memory driven by topological insulators, *Nat. Commun.*, 2021, **12**, 6251.
8 Y. Wang and H. Yang, Spin–orbit torques based on topological materials, *Acc. Mater. Res.*, 2022, **3**, 1061–1072.
9 Q. L. He, T. L. Hughes, N. P. Armitage, Y. Tokura and K. L. Wang, Topological spintronics and magnetoelectronics, *Nat. Mater.*, 2022, **21**, 15–23.
10 M. He, H. Sun and Q. L. He, Topological insulator: Spintronics and quantum computations, *Front. Phys.*, 2019, **14**, 1–16.
11 P. Huang, *et al.*, Integrated Artificial Neural Network with Trainable Activation Function Enabled by Topological Insulator-Based Spin–Orbit Torque Devices, *ACS Nano*, 2024, **18**, 29469–29478.
12 M. M. Otrokov, *et al.*, Highly-ordered wide bandgap materials for quantized anomalous Hall and magnetoelectric effects, *2D Mater.*, 2017, **4**, 025082.
13 J. Li, *et al.* Intrinsic magnetic topological insulators in van der Waals layered $MnBi_2Te_4$-family materials, *Sci. Adv.*, 2019, **5**, eaaw5685.
14 H. Zhang, W. Yang, Y. Wang and X. Xu, Tunable topological states in layered magnetic materials of $MnSb_2Te_4$, $MnBi_2Se_4$, and $MnSb_2Se_4$, *Phys. Rev. B*, 2021, **103**, 094433.
15 Y. Deng, *et al.*, Quantum anomalous Hall effect in intrinsic magnetic topological insulator $MnBi_2Te_4$, *Science*, 2020, **367**, 895–900.
16 C. Liu, *et al.*, Robust axion insulator and Chern insulator phases in a two-dimensional antiferromagnetic topological insulator, *Nat. Mater.*, 2020, **19**, 522–527.
17 N. Wang, *et al.*, Quantum-metric-induced nonlinear transport in a topological antiferromagnet, *Nature*, 2023, **621**, 487–492.
18 A. Gao, *et al.*, Layer Hall effect in a 2D topological axion antiferromagnet, *Nature*, 2021, **595**, 521–525.
19 A. Gao, *et al.*, An antiferromagnetic diode effect in even-layered $MnBi_2Te_4$, *Nat. Electron.*, 2024, 1–9.

20 M. M. Otrokov, *et al.*, Prediction and observation of an antiferromagnetic topological insulator, *Nature*, 2019, **576**, 416–422.
21 S. Qi, R. Gao, M. Chang, Y. Han and Z. Qiao, Pursuing the high-temperature quantum anomalous Hall effect in $MnBi_2Te_4/Sb_2Te_3$ heterostructures, *Phys. Rev. B*, 2020, **101**, 014423.
22 J. Wu, *et al.*, Toward 2D Magnets in the $(MnBi_2Te_4)(Bi_2Te_3)_n$ Bulk Crystal, *Adv. Mater.*, 2020, **32**, 2001815.
23 I. I. Klimovskikh, *et al.*, Tunable 3D/2D magnetism in the $(MnBi_2Te_4)(Bi_2Te_3)_m$ topological insulators family, *npj Quantum Mater.*, 2020, **5**, 54.
24 L. Ding, *et al.*, Crystal and magnetic structures of magnetic topological insulators $MnBi_2Te_4$ and $MnBi_4Te_7$, *Phys. Rev. B*, 2020, **101**, 020412.
25 R. C. Vidal, *et al.*, Topological Electronic Structure and Intrinsic Magnetization in MnBi4Te7: A Bi2Te3 Derivative with a Periodic Mn Sublattice, *Phys. Rev. X*, 2019, **9**, 041065.
26 M. Z. Shi, *et al.*, Magnetic and transport properties in the magnetic topological insulators $MnBi_2Te_4(Bi_2Te_3)_n$ (n = 1,2), *Phys. Rev. B*, 2019, **100**, 155144.
27 P. Chen, *et al.*, Tailoring the magnetic exchange interaction in $MnBi_2Te_4$ superlattices via the intercalation of ferromagnetic layers, *Nat. Electron.*, 2023, **6**, 18–27.
28 P. Chen, *et al.*, Tailoring the hybrid anomalous Hall response in engineered magnetic topological insulator heterostructures, *Nano Lett.*, 2020, **20**, 1731–1737.
29 C. Weyrich, *et al.*, Growth, characterization, and transport properties of ternary $(Bi_{1-x}Sb_x)_2Te_3$ topological insulator layers, *J. Phys.: Condens. Matter*, 2016, **28**, 495501.
30 M. H. Du, J. Yan, V. R. Cooper and M. Eisenbach, Tuning Fermi levels in intrinsic antiferromagnetic topological insulators $MnBi_2Te_4$ and $MnBi_4Te_7$ by defect engineering and chemical doping, *Adv. Funct. Mater.*, 2021, **31**, 2006516.
31 A. Gibaud, M. Chebil and T. Beuvier, X-ray reflectivity, *Surf. Sci. Tech.*, 2013, 191–216.
32 R. Yu, *et al.*, Quantized anomalous Hall effect in magnetic topological insulators, *Science*, 2010, **329**, 61–64.
33 C. Z. Chang, *et al.*, Thin films of magnetically doped topological insulator with carrier–independent long–range ferromagnetic order, *Adv. Mater.*, 2013, **25**, 1065–1070.
34 C.-Z. Chang, *et al.*, Experimental observation of the quantum anomalous Hall effect in a magnetic topological insulator, *Science*, 2013, **340**, 167–170.
35 E. D. Rienks, *et al.*, Large magnetic gap at the Dirac point in $Bi_2Te_3/MnBi_2Te_4$ heterostructures, *Nature*, 2019, **576**, 423–428.
36 J. Henk, *et al.*, Topological character and magnetism of the Dirac state in Mn-doped Bi_2Te_3, *Phys. Rev. Lett.*, 2012, **109**, 076801.
37 A. M. Shikin, *et al.*, Nature of the Dirac gap modulation and surface magnetic interaction in axion antiferromagnetic topological insulator $MnBi_2Te_4$, *Sci. Rep.*, 2020, **10**, 13226.
38 K. Edmonds, *et al.*, Surface effects in Mn $L_{3,2}$ X-ray absorption spectra from (Ga, Mn) As, *Appl. Phys. Lett.*, 2004, **84**, 4065–4067.
39 M. D. Watson, *et al.*, Study of the structural, electric and magnetic properties of Mn-doped Bi_2Te_3 single crystals, *New J. Phys.*, 2013, **15**, 103016.
40 J. Sun, S. Liu, F. Xiu and W. Liu in 2024 IEEE International Magnetic Conference-Short papers (INTERMAG Short papers). 1–2 (IEEE).
41 M. M. Otrokov, *et al.*, Unique thickness-dependent properties of the van der Waals interlayer antiferromagnet $MnBi_2Te_4$ films, *Phys. Rev. Lett.*, 2019, **122**, 107202.
42 Y.-F. Zhao, *et al.*, Even–Odd Layer-Dependent Anomalous Hall Effect in Topological Magnet $MnBi_2Te_4$ Thin Films, *Nano Lett.*, 2021, **21**, 7691–7698.
43 J.-Q. Yan, *et al.*, Evolution of structural, magnetic, and transport properties in $MnBi_{2-x}Sb_xTe_4$, *Phys. Rev. B*, 2019, **100**, 104409.
44 K. Edmonds, *et al.*, Ferromagnetic moment and antiferromagnetic coupling in (Ga, Mn) As thin films, *Phys. Rev. B: Condens. Matter Mater. Phys.*, 2005, **71**, 064418.
45 Y. Gong, *et al.*, Experimental Realization of an Intrinsic Magnetic Topological Insulator, *Chin. Phys. Lett.*, 2019, **36**, 076801.
46 S. Yang, *et al.*, Odd-Even Layer-Number Effect and Layer-Dependent Magnetic Phase Diagrams in $MnBi_2Te_4$, *Phys. Rev. X*, 2021, **11**, 011003.
47 G. van der Laan and B. Thole, Strong magnetic X-ray dichroism in 2*p* absorption spectra of 3*d* transition-metal ions, *Phys. Rev. B:Condens. Matter Mater. Phys.*, 1991, **43**, 13401.
48 G. van der Laan, Hitchhiker's guide to multiplet calculations, *Magnetism: A Synchrotron Radiation Approach*, 2006, pp. 143–199.
49 R. D. Cowan, *The theory of atomic structure and spectra*, Univ of California Press, 1981.
50 F. M. de Groot, *et al.*, 2*p* X-ray absorption spectroscopy of 3*d* transition metal systems, *J. Electron Spectrosc.*, 2021, **249**, 147061.